fluids

MDPI

Article

Structural and Hemodynamic Performance of a Polyurethane Prosthetic Aortic Valve

Celia Barba Soriano, Samikshya Neupane and Tarun Goswami *

Biomedical, Industrial and Human Factors Engineering, Wright State University, 3640 Col. Glen Hwy, Dayton, OH 45435, USA; barbasoriano.2@wright.edu (C.B.S.); neupane.36@wright.edu (S.N.)
* Correspondence: tarun.goswami@wright.edu

Abstract

Computational modeling has become an essential tool for evaluating prosthetic heart valve performance prior to experimental and clinical investigations. The objective of this study was to evaluate the structural response and hemodynamic performance of a tricuspid polyurethane prosthetic aortic valve using finite element analysis (FEA) and computational fluid dynamics (CFD). A three-dimensional valve model was developed in SolidWorks and analyzed in SimScale under physiologically representative loading conditions. The structural simulations quantified leaflet deformation, strain, and von Mises stress distributions, while the CFD simulations assessed pressure distribution, velocity fields, turbulent kinetic energy, wall shear stress, and flow streamlines through the valve in its fixed-open configuration with a k–ω SST turbulence model. The maximum leaflet displacement was 2.07 mm, with a peak von Mises stress of 1.19 MPa and a peak shear strain component (EPXY) of 6.70×10^{-2}, primarily localized near the commissural attachment regions. The CFD analysis yielded a maximum axial Y-velocity component of 2.93 m/s and a maximum three-dimensional velocity magnitude of 3.10 m/s. The simplified Bernoulli estimate based on the velocity magnitude was 38.44 mmHg (34.34 mmHg when based on the axial component); these are velocity-derived estimates rather than directly calculated CFD pressure differences. The simulations also showed localized turbulent kinetic energy and localized wall shear stress concentrations near the leaflet free edges. The combined structural and hemodynamic results indicate that the proposed polyurethane valve geometry exhibits controlled leaflet deformation and stable flow characteristics under the prescribed loading conditions, within the limits of a linear elastic leaflet model and a rigid, fixed-open CFD model that does not capture valve dynamics. These findings demonstrate the feasibility of an independent computational framework for preliminary prosthetic valve evaluation and the provide baseline data for future experimental validation and fluid–structure interaction studies.

Keywords: prosthetic aortic valve; polyurethane; finite element analysis; computational fluid dynamics; heart valve biomechanics; structural mechanics; hemodynamics

Academic Editors: Dimitrios V. Papavassiliou and Mesude Avci

Received: 9 October 2026
Revised: 17 November 2026
Accepted: 19 November 2026
Published: 21 November 2026

Copyright: © 2026 by the authors. Licensee MDPI, Basel, Switzerland. This article is an open access article distributed under the terms and conditions of the Creative Commons Attribution (CC BY) license.

1. Introduction

The aortic valve plays a critical role in maintaining unidirectional blood flow from the left ventricle to the systemic circulation [1–3]. Degenerative valve disease, congenital abnormalities, rheumatic heart disease, and age-related calcification can impair normal valve function, resulting in aortic stenosis or aortic regurgitation and ultimately requiring

valve replacement. Among congenital valve disorders, bicuspid aortic valve (BAV) is the most common abnormality, affecting approximately 1–2% of the population and frequently progressing to clinically significant valve dysfunction that requires surgical intervention [4].

Surgical aortic valve replacement remains the standard treatment for severe valvular disease. The currently available prosthetic heart valves are broadly classified as mechanical or bioprosthetic valves. Mechanical valves exhibit excellent long-term durability but require lifelong anticoagulation medication because of their thrombogenic surfaces, increasing the risk of bleeding complications [5]. In contrast, bioprosthetic valves generally provide superior hemodynamic performance and reduced thrombogenicity but are susceptible to structural valve deterioration, calcification, and limited durability, particularly in younger patients [6]. These limitations have motivated continued research into polymeric prosthetic heart valves that aim to combine the durability of mechanical valves with the favorable hemodynamic characteristics of bioprosthetic valves [7,8].

Among the polymeric materials investigated for cardiovascular applications, polyurethane has attracted considerable attention because of its flexibility, fatigue resistance, biocompatibility, and ease of fabrication [7,9]. Advances in polyurethane chemistry and manufacturing techniques have renewed interest in polymeric heart valves by improving their mechanical stability and resistance to structural degradation [10]. Experimental studies have demonstrated encouraging durability and hemocompatibility of polyurethane valve prototypes, suggesting their potential as next-generation prosthetic heart valves [7,11–13]. Nevertheless, optimization of valve geometry and mechanical performance remains essential before clinical translation.

Computational modeling has become an indispensable component of prosthetic heart valve development because it enables the detailed evaluation of valve performance before prototype fabrication or experimental testing [14–16]. Finite element analysis (FEA) is widely used to assess structural behavior, including leaflet deformation, stress, and strain under physiological loading conditions [14], whereas computational fluid dynamics (CFD) provides detailed characterization of blood flow, pressure distribution, velocity fields, turbulent kinetic energy, and wall shear stress through prosthetic valves [17–20]. Together, these computational approaches provide valuable information for evaluating valve performance while reducing development time, experimental cost, and design iterations [21].

Previous computational investigations have evaluated native aortic valves, bicuspid aortic valves, transcatheter heart valves, and commercially available prosthetic valves using FEA, CFD, and fluid–structure interaction (FSI) techniques [22]. These studies have demonstrated the importance of stress distribution, transvalvular pressure gradients, flow organization, and wall shear stress in determining valve durability and hemodynamic performance [22]. Although FSI provides detailed representation of the interaction between leaflet deformation and blood flow, it is computationally intensive and is primarily used for advanced valve optimization or patient-specific investigations [23–25].

Despite these advances, relatively few computational studies have focused specifically on polyurethane prosthetic aortic valves using independent structural and hemodynamic analyses [15,17]. In the early stages of prosthetic valve development, independent finite element analysis and computational fluid dynamics provide an efficient approach for evaluating leaflet mechanics and blood-flow characteristics separately before progressing to more computationally demanding FSI simulations or experimental validation. Such independent analyses allow designers to identify potential structural and hemodynamic limitations while reducing computational complexity during the initial design phase.

Although the principal valve dimensions were selected from published physiological and prosthetic valve data, the three-dimensional leaflet geometry was independently

reconstructed in the present study. The primary contribution of this work is the systematic computational evaluation of this independently developed polyurethane prosthetic valve using separate finite element analysis and computational fluid dynamics simulations. This computational framework enables efficient preliminary assessment of structural response and hemodynamic performance before experimental validation or more computationally intensive fluid–structure interaction analyses.

Therefore, the objective of this study was to systematically evaluate the structural response and hemodynamic performance of a tricuspid polyurethane prosthetic aortic valve using finite element analysis and computational fluid dynamics. The finite element analysis quantified leaflet displacement, stress, strain, velocity, and acceleration under physiological pressure loading, whereas the computational fluid dynamics analysis independently characterized blood flow through the valve in a prescribed fixed-open configuration by evaluating pressure distribution, velocity, turbulent kinetic energy, wall shear stress, and flow streamlines. The findings provide baseline computational data for the preliminary assessment and optimization of polyurethane prosthetic valve designs and establish a foundation for future experimental validation and fluid–structure interaction studies.

2. Methodology

2.1. Study Overview

A computational framework consisting of independent structural FEA and CFD was developed to evaluate the mechanical behavior and hemodynamic performance of a tricuspid polyurethane prosthetic aortic valve [14,17]. Three-dimensional valve geometry was created using SolidWorks 2025 (Dassault Systèmes, Vélizy-Villacoublay, France), while all structural and fluid simulations were performed using SimScale (SimScale GmbH, Munich, Germany). Structural analyses quantified leaflet deformation, strain, and stress under physiological loading conditions, whereas CFD simulations characterized pressure distribution, velocity fields, turbulent kinetic energy (TKE), wall shear stress (WSS), and flow streamlines through the prosthetic valve in its fully open configuration.

The structural and fluid analyses were deliberately uncoupled, and the CFD model represents the valve as a rigid body fixed in its open position at peak systole. This choice follows from the aim of this study, which is to screen leaflet geometry and material response at the early design stage and to generate baseline data at modest computational cost [15,21]. A coupled fluid–structure interaction (FSI) model of a thin leaflet must resolve large leaflet displacement, leaflet–leaflet contact at coaptation, and the associated fluid–mesh deformation or immersed-boundary treatment, and its results depend on the coupling scheme, contact formulation, and boundary conditions [23–26]. Such a model also needs input data that do not yet exist for this prototype, including viscoelastic leaflet properties and measured pulse-duplicator pressure and flow histories, which belong to the planned experimental phase. The quantities reported here for the open valve (peak axial velocity, velocity-derived pressure-gradient estimated, TKE, and WSS) are governed mainly by the open-valve geometry, so a rigid fixed-open model gives a first estimate of them. Valve opening and closing dynamics, regurgitation, and leaflet flutter are outside the scope of this model and are not assessed. Luraghi et al. [25] compared structural and FSI simulations of an aortic valve prosthesis and concluded that the modeling approach should be chosen according to the outcome of interest, which is the basis for the separate analyses used here.

2.2. Prosthetic Valve Geometry

The prosthetic valve geometry was designed as a tricuspid aortic valve consisting of three identical polyurethane leaflets positioned symmetrically at 120° intervals around the annulus. The geometry was developed to represent a standard surgical prosthetic valve intended for aortic valve replacement while maintaining physiological leaflet curvature and coaptation characteristics.

The principal geometric dimensions were selected based on previously published prosthetic valve designs and physiological human aortic valve dimensions reported in the literature [27,28]. The valve had an annular diameter of 25 mm, an overall valve height of 15 mm, and a uniform leaflet thickness of 0.40 mm as summarized in Table 1. Commissural attachment regions and leaflet free edges were designed to provide smooth leaflet curvature while minimizing geometric discontinuities that could artificially increase local stress concentrations.

Following completion of the CAD model, the valve geometry was exported in STEP format and imported into SimScale for structural and fluid analyses.

Table 1. Geometric parameters of the polyurethane prosthetic valve.

Parameter	Value
Annulus diameter	25 mm
Valve height	15 mm
Leaflet thickness	0.40 mm
Number of leaflets	3
Leaflet configuration	Symmetric tricuspid
Material	Polyurethane

The resulting prosthetic valve geometry used in the simulations is shown in Figure 1.

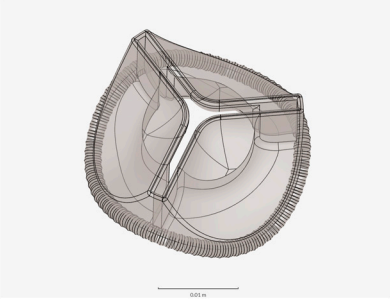


Figure 1. SolidWorks model of prosthetic aortic valve.

2.3. Material Properties

The valve leaflets were modeled as homogeneous isotropic polyurethane. Material properties representative of biomedical-grade polyurethane reported for cardiovascular applications were assigned [7,9,29] and are summarized in Table 2.

A linear elastic, isotropic description was adopted for this first-pass analysis. The model requires only a modulus, a Poisson's ratio, and a density, which are available for biomedical-grade polyurethane [7,9,29], and it allows leaflet geometries to be compared without confounding from the fitting of a more complex constitutive law. Polyurethane elastomers are nonlinear and rate-dependent at larger strains [29], and leaflets are also expected to show viscoelastic creep and stress relaxation under repeated loading. These effects, together with possible anisotropy, damage, and fatigue, are not represented, so the stresses and strains reported here are first-order estimates of the leaflet response. Since

the leaflet modulus and the thickness influence the hydrodynamic function of polyurethane valves [11], the assumed values (4 MPa and 0.40 mm) are a source of uncertainty. Hyperelastic and viscoelastic formulations calibrated to tensile tests of the final leaflet material are planned (Section 4.2).

Table 2. Material properties assigned to the polyurethane valve leaflets.

Property	Value
Density	1100 kg/m^3
Young's modulus	4 MPa
Poisson's ratio	0.48

2.4. Structural Finite Element Analysis

Structural simulations were performed using the finite element module in SimScale to evaluate leaflet deformation and stress under physiological loading conditions [14,30].

The annular ring was constrained using a fixed boundary condition to represent rigid attachment of the prosthetic valve to the aortic annulus following implantation, a commonly adopted assumption in computational heart valve mechanics. A prescribed transient pressure loading profile was applied to the ventricular surface of the valve leaflets over one simulated cardiac cycle to evaluate the structural response under cyclic loading conditions. Similar pressure-driven loading strategies have been widely employed in computational analyses of prosthetic and native aortic valves [23,24,31]. The simulation represented one cardiac cycle of 0.8 s with a time step of 0.001 s. The pressure waveform, shown in Figure 2, varied throughout the simulated cardiac cycle and served as the external mechanical load acting on the leaflet structure. The loading profile was selected to reproduce the cyclic variation in leaflet loading encountered during cardiac valve function and to assess the deformation, stress, strain, velocity, and acceleration responses of the polyurethane leaflets under transient conditions. The analysis was geometrically nonlinear (large-displacement formulation enabled), with a linear elastic material law.

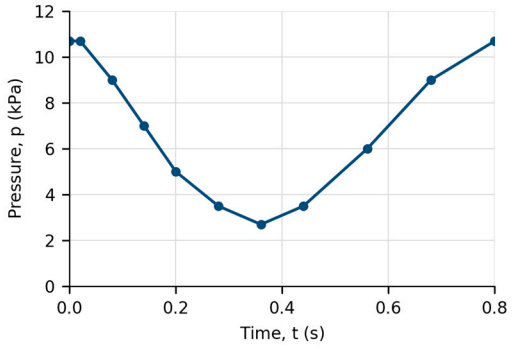


Figure 2. Time-dependent pressure loading profile applied to the ventricular surface of the prosthetic valve leaflets during the transient structural simulation. The dots represent the prescribed pressure values at discrete time points, while the solid line represents the interpolated pressure waveform.

2.5. Computational Fluid Dynamics

Hemodynamic performance was evaluated independently using CFD simulations performed in SimScale. Unlike the structural analysis, the CFD model considered only the blood domain, while the prosthetic valve was represented as a rigid, fixed-open geometry corresponding to peak systolic valve opening. Consequently, the polyurethane material properties assigned in the structural analysis were not incorporated into the CFD

simulations, allowing the hemodynamic behavior of blood flow through the prescribed valve geometry to be evaluated independently.

Blood was modeled as an incompressible Newtonian fluid with a density of 1060 kg/m^3 and dynamic viscosity of 0.0035 Pa·s, which is a commonly adopted approximation for large-vessel cardiovascular CFD simulations where shear rates remain sufficiently high for Newtonian behavior [17,32–34]. At the highest WSS predicted here (about 5 Pa), the wall shear rate is of order 1.4×10^3 s^{-1} (τ/μ), a range in which shear thinning of blood is small. Brambila-Solórzano et al. found blood rheology to be of limited relevance in aortic aneurysms [35], whereas Canbolat et al. reported WSS differences of 8.7–32.5% between non-Newtonian models and the Newtonian assumption in a thoracic aorta [36]. The WSS values reported here are therefore Newtonian estimates, and thrombogenicity was not evaluated.

Turbulence was modeled with the k–ω SST Reynolds-averaged model. A Reynolds-averaged formulation provides the mean flow and the modeled turbulent kinetic energy reported in Section 3.2.2 at a cost compatible with a transient simulation of one cardiac cycle. In aortic hemodynamics, laminar and several RANS formulations give similar mean flow and WSS [36], and the choice of turbulence model had little effect on results in aortic aneurysm simulations [35]. TKE and WSS from the present model are model-dependent quantities and are therefore interpreted as relative indicators of flow disturbance. A turbulence-model sensitivity study was not performed.

A prescribed transient velocity waveform representing pulsatile left ventricular outflow was applied at the inlet using a spatially uniform velocity profile. A transient pressure waveform representative of physiological aortic pressure was prescribed at the outlet. The inlet velocity peaks at 1.5 m/s at t = 0.24 s and returns to zero at the end of the 0.8 s cycle, and the outlet gauge pressure varies between 10.7 kPa (80 mmHg) and 16.0 kPa (120 mmHg) (Figure 3). The inlet condition is an idealized pulsatile velocity waveform representing physiological aortic outflow, and the outlet condition is a time-dependent pressure waveform representing physiological aortic pressure. The choice of pulsatile boundary conditions was informed by published computational and physiological studies of aortic hemodynamics [37–40]. The waveforms are idealized representations and not patient-specific measurements. The combination of velocity inlet and pressure outlet boundary conditions is widely used in cardiovascular CFD simulations because it provides physiologically realistic pressure–flow relationships while maintaining numerical stability. No-slip boundary conditions were imposed on all rigid solid surfaces [17,37,41]. The inlet velocity and outlet pressure waveforms used in the CFD analysis are shown in Figure 3. The simulations evaluated static pressure, velocity distribution, turbulent kinetic energy (TKE), wall shear stress (WSS), and velocity streamlines to characterize the hemodynamic performance of the prosthetic valve.

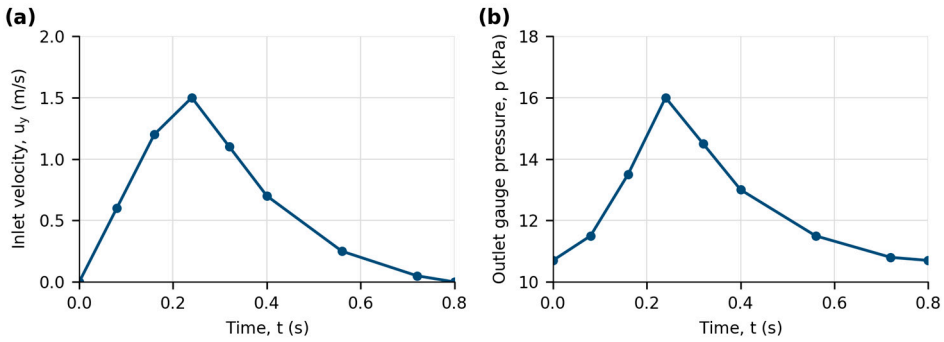


Figure 3. Time-dependent boundary-condition waveforms over one cardiac cycle: (**a**) velocity (m/s) and (**b**) pressure (Pa). Symbols represent the prescribed input values, while solid curves indicate shape-preserving interpolation.

The prescribed inlet velocity and outlet pressure waveforms were selected to reproduce the transient physiological loading environment experienced by the aortic valve during one cardiac cycle and were implemented as independent boundary conditions for the CFD analysis. Similar combinations of transient velocity inlet and pressure outlet boundary conditions have been widely employed in computational investigations of prosthetic and native aortic valve hemodynamics [26,37,41].

2.6. Mesh Generation

The computational domains were discretized using unstructured tetrahedral meshes with local refinement near the leaflet surfaces, free edges, and commissural attachment regions, where elevated structural and flow gradients were expected. A representative computational mesh is shown in Figure 4.

Near-wall resolution was set to support the WSS predictions. The fluid domain was resolved at solid surfaces with 15 prism (inflation) layers, a first-layer thickness of 0.010 mm, and a growth ratio of 1.20, giving a total inflation thickness of about 0.72 mm and a dimensionless wall distance y^+ of approximately 1 at peak flow. This near-wall resolution is consistent with a wall-resolved application of the k–ω SST model.

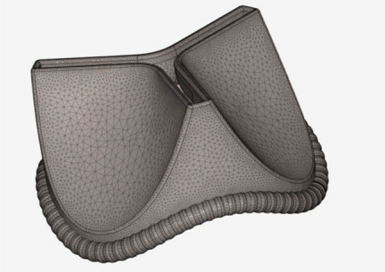


Figure 4. Representative unstructured tetrahedral mesh of the prosthetic valve.

Mesh independence was evaluated [42] separately for the structural and fluid models, each with three progressively refined meshes. The structural meshes contained approximately 4.2, 5.8, and 8.9 million elements. Between the medium and fine meshes the maximum displacement changed by 1.45% and the maximum von Mises stress by 0.84% (Table 3). The fluid meshes contained 325,000, 585,400, and 1,100,000 cells (70,000, 127,000, and 240,000 nodes), and peak axial velocity, maximum WSS, and maximum TKE were compared (Table 4). Between the medium and fine fluid meshes these quantities changed by 1.7%, 2.4%, and 2.5%, respectively. The grid convergence index of the fine fluid mesh, computed by the procedure of Celik et al. [42] with the cell-count refinement ratios of 1.22 (coarse to medium) and 1.23 (medium to fine), was 1.5% for peak axial velocity, 2.9% for maximum WSS, and 3.3% for maximum TKE, with apparent orders of 4.2, 3.3, and 3.1. The medium meshes were selected for all simulations because they balance numerical accuracy and computational cost, and all results in Section 3 were obtained with them.

Table 3. Mesh independence results for the structural model.

Mesh Level	Elements	Maximum Total Displacement (mm)	Displacement Change (%)	Maximum von Mises Stress (MPa)	Stress Change (%)
Coarse	4,200,000	2.01	—	1.14	—
Medium	5,800,000	2.07	2.99	1.19	4.39
Fine	8,900,000	2.10	1.45	1.20	0.84

Table 4. Mesh independence results for the fluid model.

Mesh Level	Number of Cells	Maximum Axial Y-Component Velocity (u_y) (m/s)	Maximum WSS (Pa)	Maximum TKE (m^2/s^2)
Coarse	325,000	2.82	4.78	5.82×10^{-4}
Medium	585,400	2.93	5.00	6.08×10^{-4}
Fine	1,100,000	2.98	5.12	6.23×10^{-4}

2.7. Post-Processing

Simulation results were post-processed within SimScale. Displacement, von Mises stress, and strain were evaluated over the leaflet surface at the instant of maximum applied pressure (Figure 2), and velocity and acceleration over the full cycle. Pressure, velocity, TKE, and WSS were evaluated at t = 0.24 s (peak inlet velocity) on the planes indicated in the figure captions. The CFD velocity results distinguish the maximum axial Y-component (u_y = 2.93 m/s) from the maximum three-dimensional velocity magnitude ($|v|$ = 3.10 m/s), both reported at t = 0.24 s. The simplified Bernoulli relation $\Delta P \approx 4V^2$ (ΔP in mmHg, V in m/s) was applied to the maximum velocity magnitude, giving 38.44 mmHg. For comparison, applying the same expression to the axial component gives $4u_y^2$ = 34.34 mmHg. These are velocity-derived estimates and not pressure differences calculated from area-averaged upstream and downstream CFD pressures. WSS is the tangential stress exerted by the blood on the valve surface, and TKE is the modeled turbulent kinetic energy of the turbulence model.

Structural analyses included:

- Leaflet deformation
- Von Mises stress
- Total nonlinear strain (EPXY shear component)

Fluid analyses included:

- Pressure contours
- Velocity contours
- Turbulent kinetic energy
- Wall shear stress
- Velocity streamlines

3. Results

3.1. Structural Performance of the Polyurethane Prosthetic Valve

3.1.1. Displacement

The transient structural simulations showed a deformation pattern of the polyurethane prosthetic valve under physiological loading conditions. The displacement contours

(Figure 5a) indicate that deformation was primarily concentrated near the leaflet free edges, while the commissural attachment regions remained mechanically constrained by the fixed annular boundary condition. The gradual transition in displacement from the commissures toward the leaflet center shows a gradual spatial variation in displacement in the present model.

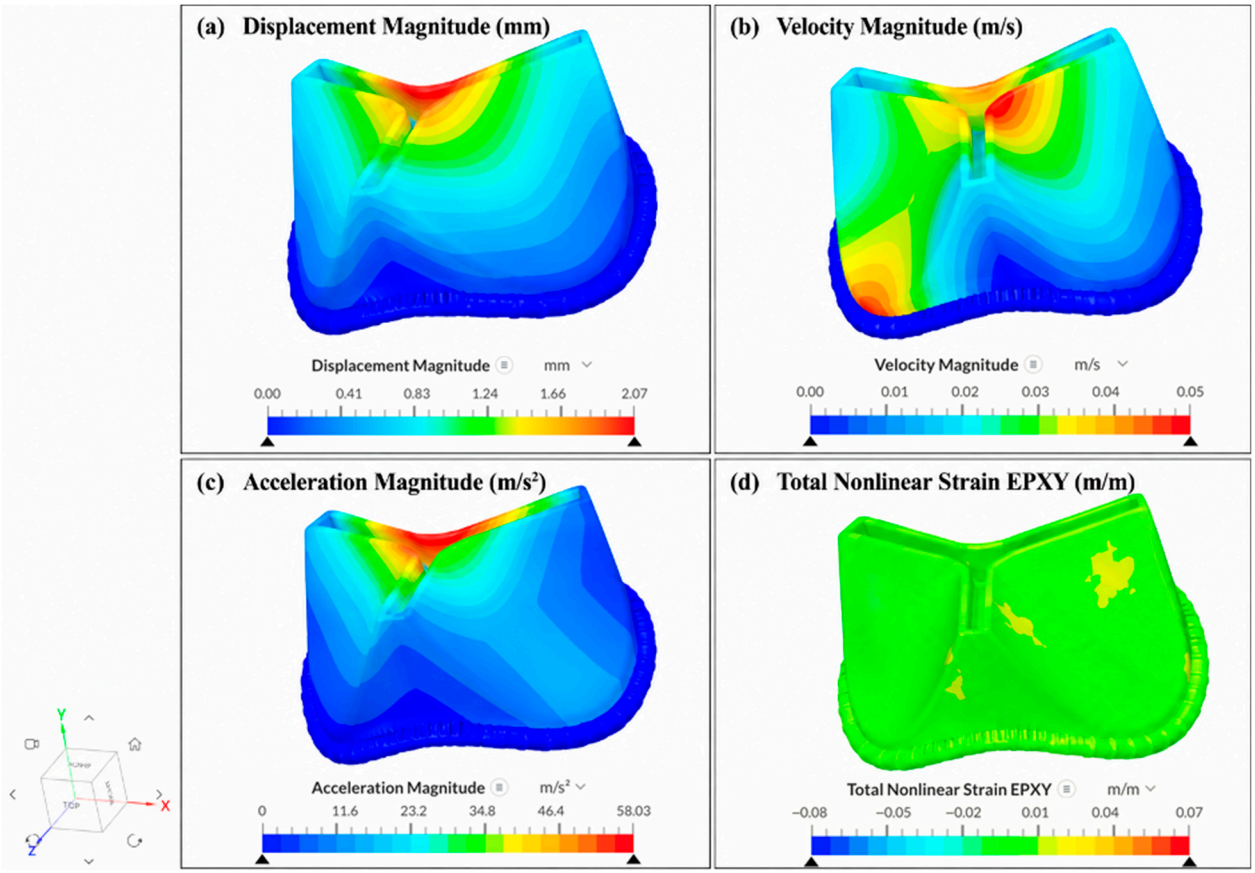


Figure 5. Transient structural response of the polyurethane prosthetic valve under physiological loading conditions: (**a**) displacement magnitude, (**b**) velocity magnitude, (**c**) acceleration magnitude, and (**d**) total nonlinear shear strain component (EPXY). The color bars indicate the corresponding values in the displayed units. The black triangular markers at the ends of the color bars indicate the minimum and maximum values, respectively. The coordinate orientation is indicated by the shared X_Y_Z coordinate triad.

The maximum displacement magnitude was 2.07 mm, occurring at the time of maximum applied pressure during the simulated loading cycle. This displacement represents approximately 8.3% of the 25 mm annular diameter, quantifying the deformation predicted under the applied pressure. The symmetric deformation pattern observed across the leaflet surface describes the deformation distribution within the modeled geometry.

The absence of localized excessive displacement indicates that the polyurethane material provides sufficient flexibility to accommodate physiological loading while maintaining the stiffness required for stable valve function.

Within this linear elastic model, no excessive localized deformation was observed under the prescribed loading; this result does not establish long-term mechanical stability or fatigue resistance.

3.1.2. Velocity and Acceleration Distribution

The velocity and acceleration contours are presented in Figure 5b and Figure 5c, respectively. The leaflet velocity magnitude reached a maximum of 4.997×10^{-2} m/s (Figure

5b), located in the lower part of the leaflet next to the annular attachment, and the acceleration magnitude reached a maximum of 58.03 m/s^2 (Figure 5c) at the free edge. The reported velocity maximum is located near the annular attachment in the displayed structural contour; its mechanical significance cannot be established from this contour alone.

Similarly, the acceleration distribution exhibited localized peaks near the leaflet free edge, corresponding to regions undergoing rapid changes in displacement during the transient loading cycle. The smooth spatial variation in both velocity and acceleration describes the modeled response over the single prescribed loading cycle and does not establish long-term dynamic stability.

These results describe the simulated leaflet velocity and acceleration patterns during one prescribed loading cycle.

3.1.3. Strain Distribution

The nonlinear strain distribution (Figure 5d) demonstrated relatively uniform deformation throughout the leaflet surface with localized increases near the commissural attachment regions and along the leaflet belly. The plotted quantity is the total nonlinear shear strain component EPXY, which ranged from -8.27×10^{-2} to 6.70×10^{-2} (Figure 5d), a peak magnitude of about 8%. This is a single tensor component and not an equivalent strain. It is lower than the maximum in-plane principal strains of about 20–40% reported at valve closure in a hyperelastic simulation of a polymeric leaflets [43].

The strain contours indicate that mechanical deformation is distributed over a broad leaflet area rather than being confined to isolated locations. This spatial pattern characterizes the load response in the present simulation; it does not establish a reduced risk of localized material fatigue.

Overall, the strain distribution indicates that, within this linear elastic model, no excessive localized deformation was observed under the prescribed loading conditions.

3.1.4. Stress Distribution

The von Mises stress distribution is illustrated in Figure 6a, while the Cauchy shear stress components XZ (SIXZ) and XY (SIXY) are shown in Figure 6b and 6c, respectively.

The von Mises stress contours reveal that stresses were predominantly concentrated near the commissural attachment regions, with substantially lower stress levels throughout the central leaflet body. The maximum von Mises stress reached 1.19 MPa (color scale maximum 1.194 MPa, Figure 6a), occurring at the time of maximum applied pressure during the simulated loading cycle. This stress concentration is expected because the commissures serve as the primary load-transfer regions between the flexible leaflets and the supporting annulus.

The Cauchy shear stress components were relatively uniform across most of the leaflet surface and ranged from −0.386 to 0.355 MPa for SIXZ (Figure 6b) and from −0.234 to 0.229 MPa for SIXY (Figure 6c). No excessive stress concentrations were observed within the central leaflet region, describing the spatial distribution of stresses within the modeled valve.

The combined stress analyses characterize the distribution of stress under the prescribed loading conditions. Although the stress field provides useful information for identifying regions for further investigation, improved structural durability during repeated cardiac cycles cannot be established without fatigue or damage analysis and experimental validation [44].

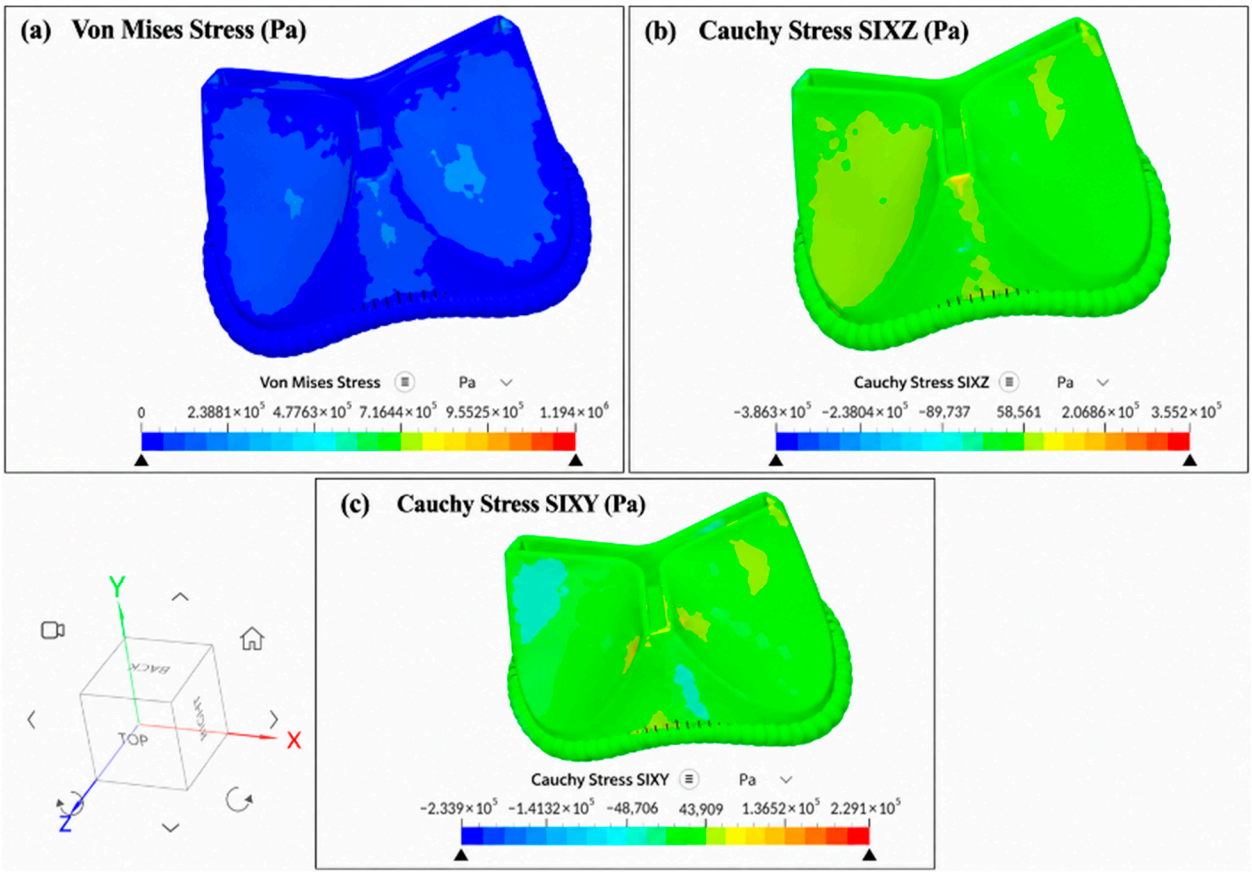


Figure 6. Stress distribution within the polyurethane prosthetic valve leaflets: (**a**) von Mises stress, (**b**) Cauchy shear stress component XZ (SIXZ), and (**c**) Cauchy shear stress component XY (SIXY). The coordinate orientation is indicated by the shared X, Y, Z coordinate triad.

3.2. Hemodynamic Performance

3.2.1. Pressure Distribution

The static pressure distribution within the computational flow domain of the fixed-open prosthetic valve is presented in Figure 7 at three axial cutting planes: (a) the base-position plane, (b) the plane through the leaflets, and (c) the valve-opening plane. The contours were obtained at t = 0.24 s, corresponding to peak prescribed inlet velocity.

The pressure contours illustrate spatial variations through the flow passage. At the base-position plane (Figure 7a), the displayed pressure ranges from 8.23 to 12.94 kPa. At the leaflet cutting plane (Figure 7b), the range is 9.25–10.87 kPa. Local variations near the leaflet surfaces are consistent with flow acceleration through the three channels formed by the fixed-open valve geometry.

At the valve-opening plane (Figure 7c), the displayed pressure ranges from 9.45 to 10.78 kPa and shows a relatively smooth spatial distribution across the flow passage. These observations are limited to the prescribed fixed-open CFD model and do not independently establish superior valve performance.

The three panels depict different axial positions at the same simulation time (t = 0.24 s). Each uses its own numerical color scale; therefore, identical colors across panels do not necessarily represent identical pressure values. The displayed local pressure distributions are not used to calculate a transvalvular pressure gradient.

Overall, the three flow-passage contours show spatial pressure variations near the leaflet surfaces and valve opening. These qualitative observations describe the prescribed fixed-open CFD configuration and do not establish reduced pressure disturbances or superior hemodynamic performance.

The maximum axial Y-component of velocity was 2.93 m/s, while the reported maximum three-dimensional velocity magnitude at t = 0.24 s was 3.10 m/s. The simplified Bernoulli expression applied to the maximum velocity magnitude gives $\Delta P \approx 4(3.10)^2 = 38.44$ mmHg; the corresponding axial-component-based estimate is $4(2.93)^2 = 34.34$ mmHg. The component-based estimate is 10.7% lower than the magnitude-based estimate. Both values are velocity-derived approximations, not transvalvular pressure differences computed from area-averaged CFD pressures and should not be used alone to classify clinical stenosis severity [1].

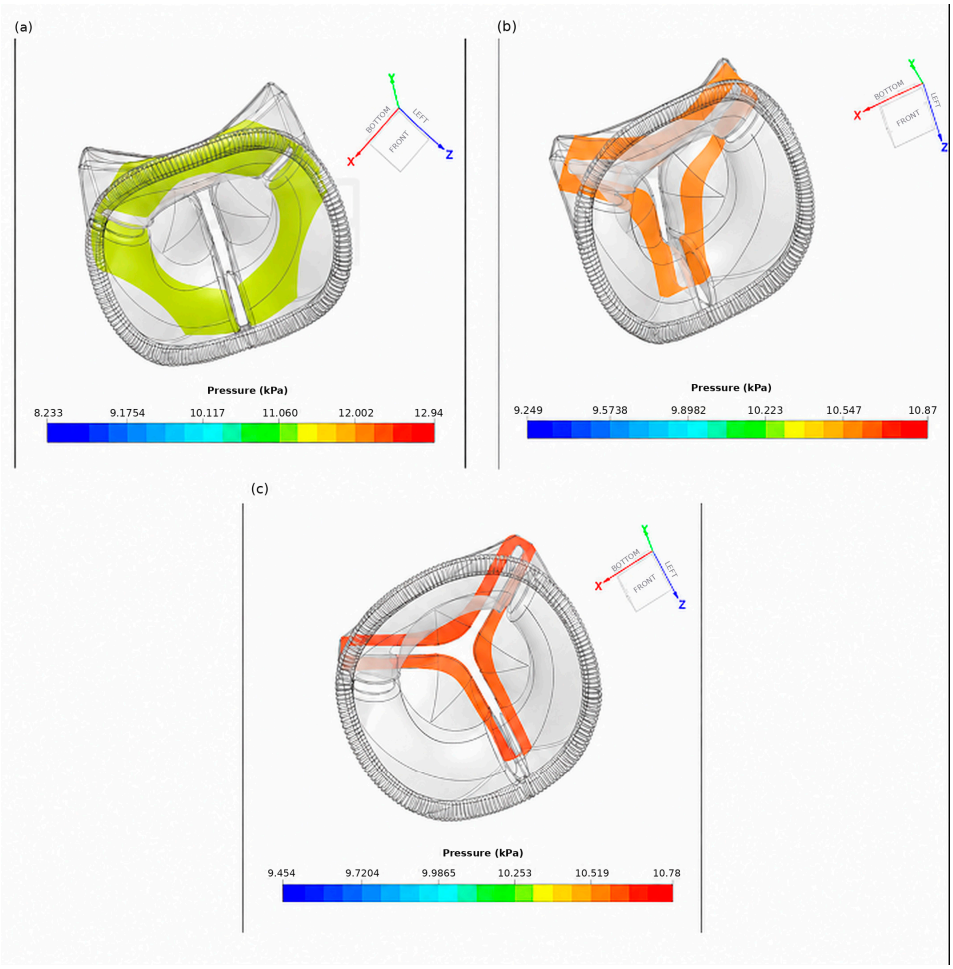


Figure 7. Static pressure contours (kPa) for the fixed-open prosthetic valve at t = 0.24 s: (**a**) base-position cutting plane, (**b**) leaflet cutting plane, and (**c**) valve-opening cutting plane. Each panel has its own numerical color scale. The orientation cube indicates the *X*, *Y*, and *Z* axes.

3.2.2. Turbulent Kinetic Energy Distribution

The turbulent kinetic energy (TKE) distribution within the computational flow domain is presented in Figure 8, illustrating the turbulence characteristics in the fixed-open valve configuration at the (a) upstream leaflet region, (b) leaflet junction, (c) jet formation region, (d) downstream aortic region, and (e) the overall flow field.

Because the CFD analysis was performed independently of the structural simulation, the valve leaflets were maintained in their designed open position throughout the simulation, and only the blood domain was considered in the hemodynamic analysis. Consequently, the observed turbulent kinetic energy reflects the flow behavior through the fixed prosthetic valve geometry rather than turbulence generated by leaflet motion.

The results demonstrate that turbulent kinetic energy remained predominantly low throughout the computational domain, with localized increases confined to the leaflet

junctions, commissural regions, and the developing flow jet immediately downstream of the valve orifice. These localized regions correspond to areas of increased flow acceleration and elevated velocity gradients produced by the valve geometry.

Minimal turbulent activity was observed in the upstream region (Figure 8a), indicating relatively uniform inflow conditions before the fluid entered the valve orifice. As the blood accelerated through the three leaflet openings, localized increases in turbulent kinetic energy developed near the leaflet junctions (Figure 8b,c), where adjacent flow streams interacted and generated localized shear layers. Further downstream (Figure 8d), the turbulent kinetic energy gradually decreased as the jet expanded into the downstream flow region, indicating progressive dissipation of flow disturbances.

The overall TKE distribution (Figure 8e) demonstrates that elevated turbulence remained confined to small regions surrounding the valve orifice, while the majority of the computational domain exhibited negligible turbulent kinetic energy. The maximum turbulent kinetic energy was approximately 6.08×10^{-4} m^2/s^2, suggesting that the prosthetic valve generated only limited turbulence under the prescribed physiological flow conditions.

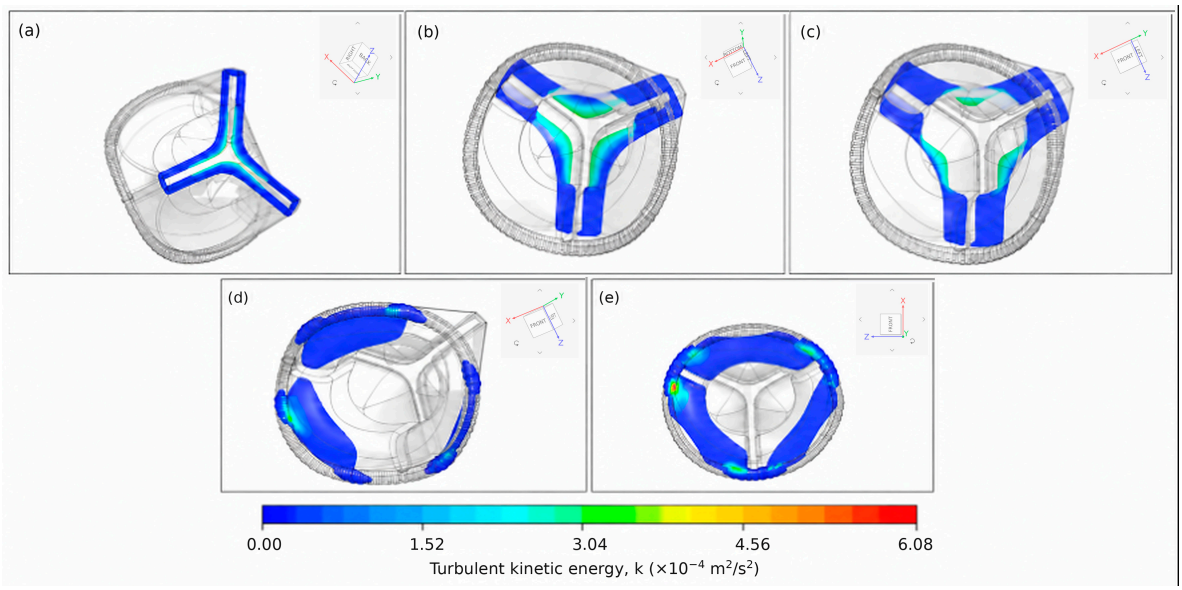


Figure 8. Turbulent kinetic energy distribution within the valve flow field in fixed-open configuration: (**a**) upstream leaflet region, (**b**) leaflet junction, (**c**) jet formation region, (**d**) downstream aortic region, (**e**) overall turbulent kinetic energy distribution. The orientation cube with the coordinate axes (X, Y, Z) is shown in each panel.

3.2.3. Velocity Distribution

The distribution of velocity within the computational flow domain is presented in Figure 9, illustrating the evolution of blood flow through the prosthetic valve in its fixed-open configuration at the (a) annular and upstream region, (b) leaflet channel region, (c) jet formation region, (d) leaflet structures, and (e) downstream flow region.

The CFD simulations predicted a gradual increase in flow velocity as blood entered the prosthetic valve from the upstream region (Figure 9a). The velocity distribution remained relatively uniform before reaching the leaflet openings, indicating stable inflow conditions and symmetric entrance of the blood into the valve.

As the flow passed through the three leaflet channels (Figure 9b), the velocity increased due to the reduction in effective flow area created by the fixed-open valve geometry. Localized regions of higher velocity developed adjacent to the leaflet surfaces, corresponding to areas where the blood accelerated through the narrow flow passages.

The highest positive axial (Y-direction) velocity components were observed within the jet formation region immediately downstream of the valve orifice (Figure 9c), where the accelerated blood streams merged to form the central transvalvular jet. The CFD simulations predicted a maximum Y-component of 2.93 m/s, whereas the separately obtained maximum three-dimensional velocity magnitude was 3.10 m/s at the same time step. The axial acceleration reflects flow through the reduced effective area of the fixed-open geometry. Since the CFD analysis was performed using a prescribed fixed-open valve configuration rather than a fully coupled FSI model, the velocity field represents blood flow under the specified boundary conditions and should not be interpreted as leaflet opening dynamics. Higher axial velocity components were concentrated in the central jet, with lower values in surrounding flow regions.

The velocity distribution along the leaflet structures (Figure 9d) demonstrates smooth acceleration of the blood along the flow channels without abrupt changes in flow direction. Downstream of the prosthetic valve (Figure 9e), the velocity gradually decreased as the jet expanded into the larger flow domain, indicating progressive redistribution of kinetic energy and stabilization of the downstream flow field.

Overall, the predicted Y-velocity component ranged from −0.385 to 2.93 m/s (Figure 9), with negative values indicating localized reverse axial flow. No abrupt flow changes were observed in the displayed contours of this prescribed fixed-open CFD model; this observation does not establish long-term hemodynamic performance.

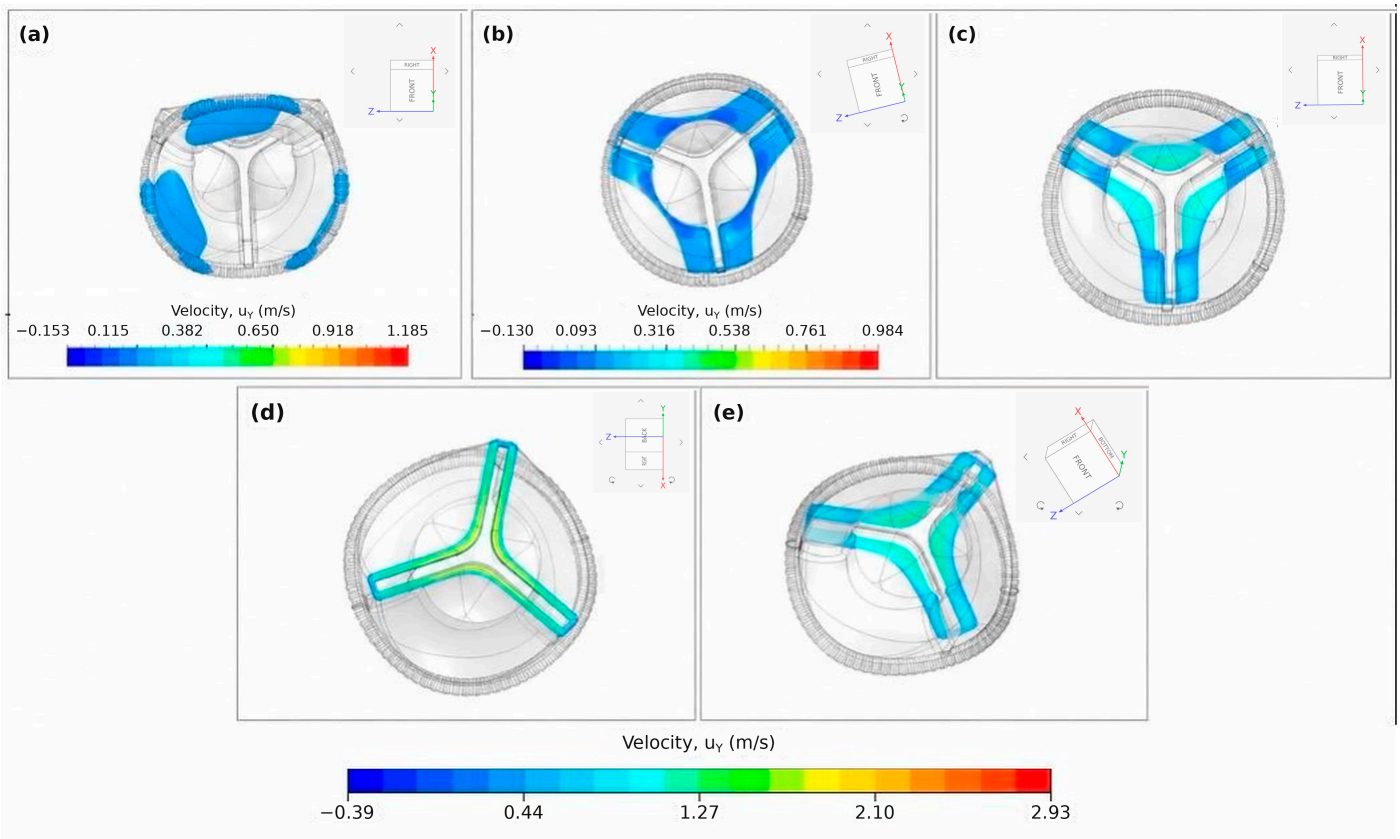


Figure 9. Velocity Y-component distribution through the prosthetic valve in fixed-open configuration: (**a**) annular and upstream region, (**b**) leaflet channel region, (**c**) during jet formation through the valve opening, (**d**) leaflet structures, (**e**) downstream of the prosthetic valve. The orientation cube with the coordinate axes (X, Y, Z) is shown in each panel.

3.2.4. Wall Shear Stress Distribution

The wall shear stress (WSS) distribution predicted by the CFD simulations is presented in Figure 10 for the prosthetic valve in its fixed-open configuration. Wall shear stress represents the tangential force exerted by the flowing blood on the valve surfaces and provides an important indicator of local hemodynamic loading.

The WSS contours demonstrate that the majority of the leaflet surfaces experienced relatively low wall shear stress, while localized regions of elevated WSS developed near the leaflet free edges, commissural junctions, and the valve orifice where the blood accelerated through the three flow channels. These localized increases correspond to regions of higher velocity gradients generated by the fixed valve geometry.

The maximum wall shear stress reached 5.00 Pa (Figure 10, contour scale 0–5 Pa), with the highest values (red) along the leaflet edges and commissural walls. In contrast, the central leaflet surfaces exhibited comparatively lower wall shear stress, indicating that the blood flow remained well distributed across the prosthetic valve without producing excessive localized surface loading. These values are consistent with physiological systolic flow conditions [45] while the central parts of the leaflets remained at low shear.

Overall, the wall shear stress distribution suggests that the fixed-open valve geometry promotes relatively uniform hemodynamic loading while limiting high-shear regions to the immediate vicinity of the flow acceleration zones. Such localized WSS patterns are consistent with the expected hemodynamic behavior of prosthetic aortic valves under physiological systolic flow conditions.

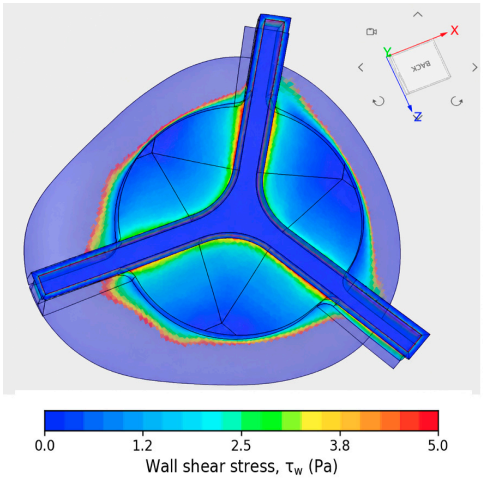


Figure 10. Wall shear stress distribution on the prosthetic valve surfaces in the fixed-open configuration. The orientation cube with the coordinate axes (X, Y, Z) is shown in the Figure.

3.2.5. Three-Dimensional Flow Visualization

The velocity streamlines obtained from the CFD simulations are shown in Figure 11, illustrating the overall flow organization through the prosthetic valve under physiological systolic conditions.

The streamline patterns indicate that blood entered the computational domain with a relatively uniform flow profile before accelerating through the three leaflet channels formed by the fixed-open valve geometry. As the flow passed through the valve orifice, the individual flow streams merged to form a central transvalvular jet that remained well organized downstream of the valve.

The streamlines in Figure 11 are colored by the Y-velocity component on a scale of −0.385 to 2.93 m/s and lie mainly in the lower part of this scale, converging smoothly through the valve without large-scale flow separation [40]. The negative end of the scale indicates localized reverse flow elsewhere in the domain. Minor streamline curvature was

observed immediately downstream of the leaflet tips as the jet expanded into the downstream flow region, reflecting the gradual redistribution of momentum following passage through the valve orifice.

Overall, the streamline distribution confirms that the prosthetic valve promotes stable forward flow with symmetric jet formation and minimal flow disturbance throughout the computational domain. These observations are consistent with the pressure, velocity, and turbulent kinetic energy distributions presented in the preceding sections. The principal structural and hemodynamic simulation results are summarized in Table 5.

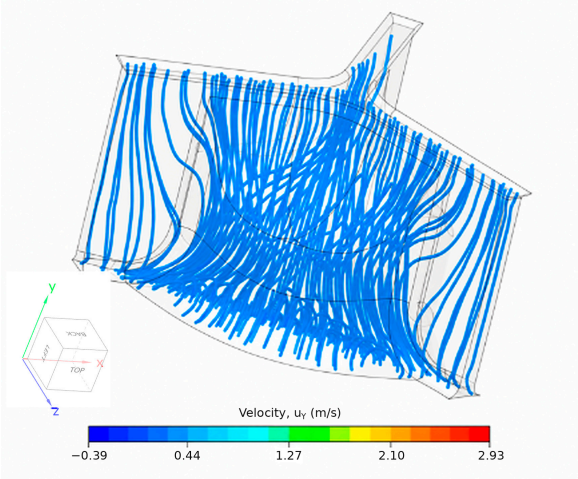


Figure 11. Velocity streamlines (Y-component) through the prosthetic valve in its fixed-open configuration. The orientation cube with the coordinate axes (X, Y, Z) is shown in the Figure.

Table 5. Summary of structural and hemodynamic simulation results.

Parameter	Predicted Value	Simulation
Maximum leaflet displacement	2.07 mm	FEA
Peak shear strain component (EPXY)	6.70×10^{-2}	FEA
Maximum von Mises stress	1.19 MPa	FEA
Maximum axial Y-velocity component, u_y	2.93 m/s	CFD
Maximum turbulent kinetic energy	6.08×10^{-4} m²/s²	CFD
Maximum wall shear stress	5.0 Pa	CFD
Estimated magnitude-based Bernoulli gradient ($4v^2$)	38.44 mmHg	CFD-derived
Maximum three-dimensional velocity magnitude, $\|v\|$	3.10 m/s	CFD
Axial-component Bernoulli estimate ($4u_y^2$)	34.34 mmHg	Velocity-derived

4. Discussion

The present study employed two independent computational approaches to evaluate the performance of a tricuspid polyurethane prosthetic aortic valve under physiological loading conditions. FEA was performed to assess the mechanical response of the polyurethane leaflets, whereas CFD was conducted independently to characterize blood flow through the valve in its prescribed rigid, fully open configuration. This approach enabled separate evaluation of structural response and hemodynamic performance while maintaining computational efficiency during the preliminary stages of prosthetic valve design.

The structural analysis showed controlled leaflet deformation with maximum displacement occurring near the free edges, while the highest stresses and strains were

localized at the commissural attachment regions. This mechanical behavior is expected because the commissures represent the primary load-transfer interfaces between the flexible leaflets and the supporting annulus [44]. Under physiological pressure loading, bending and tensile stresses naturally accumulate at these constrained regions, whereas the central leaflet body undergoes comparatively uniform deformation. Within this linear elastic model, no excessive localized deformation was observed away from the principal stress-concentration regions under the prescribed loading; long-term structural stability was not evaluated. The localization of elevated stress near the commissural attachment regions is consistent with previous computational and experimental investigations showing that leaflet geometry and commissural constraint strongly influence stress concentration [46]. Li and Sun reported stress concentrations near the commissural attachment regions associated with leaflet geometry optimization, consistent with the maximum von Mises stress of 1.19 MPa predicted in the present study [30]. More recently, Stanová et al. reported that the highest leaflet stresses in several transcatheter valve designs occurred predominantly near the upper leaflet edges and commissures, with lower stresses across much of the leaflet body [47]. Although these studies examined transcatheter bioprostheses rather than a polyurethane surgical valve, the regional stress patterns are comparable to those predicted in the present analysis. The present findings therefore support the interpretation that the commissural regions are the principal load-transfer zones of the modeled leaflet geometry, while the remaining leaflet area undergoes comparatively distributed deformation.

The independent CFD simulations demonstrated a progressive pressure reduction as blood accelerated through the fixed-open prosthetic valve geometry. This pressure gradient resulted in the formation of a well-defined transvalvular jet downstream of the valve orifice, where the highest velocities were observed. The increase in velocity is consistent with conservation of mass and the conversion of pressure energy into kinetic energy as blood passes through the reduced effective flow area created by the open valve geometry. Downstream of the valve, the velocity gradually decreased as the jet expanded into the larger flow domain, indicating progressive momentum redistribution and recovery of the flow field. The pressure reduction and development of a central transvalvular jet are consistent with the fundamental flow behavior reported in previous computational studies of aortic valve prostheses [48]. Hsu et al. demonstrated that coupled fluid–structure interaction simulations reproduce physiological transvalvular flow acceleration while showing that arterial wall deformation influences the downstream hemodynamic environment [24]. Similarly, Kamensky et al. reproduced transvalvular jet formation and downstream flow organization using an immersogeometric fluid–structure interaction framework for bioprosthetic valves [32,49]. The present CFD analysis differs from these studies because the valve geometry was maintained in a rigid, fully open configuration and only the blood domain was solved. Nevertheless, the observed sequence of flow contraction, jet acceleration, and downstream expansion is consistent with the established hemodynamic behavior of functioning prosthetic aortic valves. Overall, the present independent CFD simulations reproduced pressure reduction, central jet formation, and downstream velocity recovery consistent with previous computational investigations of prosthetic aortic valves. Although those studies primarily employed fluid–structure interaction or patient-specific models, the comparable flow organization observed here supports the proposed valve geometry's ability to maintain physiologically realistic transvalvular hemodynamics. Similar central jet formation and downstream velocity recovery have been reported in computational investigations of prosthetic aortic valves using fluid–structure interaction and high-fidelity CFD models, although those studies additionally account for leaflet motion and arterial compliance [24,32].

Since the model is not validated against in vitro measurements, the predictions were compared with published bench data for polymeric valves, keeping in mind that those valves differ in size, polymer, flow conditions, and test fluid. The maximum axial Y-velocity component of 2.93 m/s is numerically close to the in vitro maximum velocities at rest of 3.42 m/s for a 21 mm xSIBS trileaflet valve and 2.96 m/s for a 21 mm Carpentier–Edwards Perimount Magna tissue valve at 70 beats/min and 5.6 L/min [50]. In that study, the lower effective orifice area of the polymeric valve corresponded to a peak velocity about 15% higher than that of the tissue valve, although these different velocity definitions limit direct comparison; flow velocity in the present valve is expected to depend on leaflet thickness and modulus, as also shown by Bernacca et al. [11]. The axial component-based Bernoulli estimate of 34.34 mmHg is numerically of the same order as the peak systolic pressure difference of 30.09 ± 4.7 mmHg measured in pulsatile tests of 23 mm trileaflet styrenic block copolymer valves [51], although that value is a measured pressure difference and the present value is a Bernoulli estimate from velocity. Mean gradients reported for polymeric valves, 20.91 mmHg for the xSIBS valve [50] and 9–12 mmHg for a siloxane poly(urethane-urea) transcatheter valve in a 24 mm fixture [52] are not comparable with a peak value, and a mean gradient was not computed here. Particle image velocimetry of the latter valve showed a central systolic jet, with high-velocity gradients confined to the jet and leaflet tips and no persistent stagnation at the leaflets [52], which agrees with the central jet and the confinement of high WSS to the leaflet edges in the present simulations. Further in vitro studies of polymeric valves are reviewed in [7,43,53] and include hemodynamic and durability testing of polymeric transcatheter valves [12,13,54]. Recent in vitro work agrees that leaflet thickness governs the systolic performance of polymeric valves. In 18 mm bioinspired siloxane-based polyurethane valves of 110–200 μm thickness, the effective orifice area ranged from 1.05 to 1.35 cm^2 and thinner leaflets opened more widely [55], and a review of polymeric valve testing reports mean gradients rising from 8 to 25 mmHg as leaflet thickness increased from 0.24 to 0.46 mm [7,11]. The leaflet thickness of the present valve (0.40 mm) lies in the upper part of this range, so a relatively high gradient is expected, although a mean gradient was not computed here. FSI simulations of polymeric valves further indicate that, for a leaflet modulus above that of xSIBS (2.8 MPa), a thickness below about 0.2 mm is needed to meet the regurgitant fraction requirement [43]. The 0.40 mm thickness and 4 MPa modulus used here may therefore be too thick for acceptable closing performance, which the present model cannot assess. FSI models of heart valves built with the dynamic mesh method in Fluent have been validated against in vitro data [56], and reviews of cardiac CFD identify experimental validation, for example, by particle image velocimetry or phase-contrast MRI, as a requirement for quantitative use [57]. Experimental and numerical studies of thoracic aortic flow have also supported the Newtonian assumption for large arteries [58]. The comparison is qualitative. Quantitative validation requires in vitro pulse-duplicator tests under ISO 5840-2 conditions [59], and the present values should be read as design-stage estimates.

The CFD simulations also demonstrated that turbulent kinetic energy remained localized near the leaflet junctions and immediately downstream of the valve orifice, where increased velocity gradients generated localized shear layers. Similarly, elevated wall shear stress was confined primarily to the leaflet free edges and commissural regions, while the majority of the computational domain exhibited relatively low hemodynamic loading. The limited spatial extent of elevated turbulent kinetic energy and wall shear stress suggests smooth flow organization through the prosthetic valve without widespread flow disturbance or excessive energy dissipation. Becsek et al. similarly reported localized regions of elevated shear adjacent to the developing systolic jet. In contrast, the majority of the downstream flow exhibited substantially lower turbulence levels, which is consistent with the present prediction of a maximum WSS of approximately 5 Pa and

highly localized TKE [33]. They also reported elevated shear stresses in regions influenced by the turbulent jet. Although the present model does not include the ascending aorta or dynamic leaflet flutter, the spatial localization of increased turbulent kinetic energy near the orifice and the confinement of higher wall shear stress to regions of strong velocity gradient follow the same fluid-mechanical mechanism. These observations indicate that the observed TKE and WSS patterns result primarily from jet shear-layer development and downstream dissipation rather than widespread instability throughout the computational domain.

The observed pressure reduction and velocity acceleration are consistent with classical fluid-mechanical behavior during flow through a converging passage. As blood enters the reduced effective flow area created by the valve orifice, conservation of mass requires an increase in local velocity, while Bernoulli's principle predicts a corresponding decrease in static pressure. Immediately downstream of the valve, the accelerated jet undergoes gradual expansion, producing velocity recovery and progressive pressure redistribution. Localized shear layers develop between the high-velocity jet and surrounding slower-moving fluid, explaining the spatial localization of turbulent kinetic energy and wall shear stress observed in the present simulations.

The streamline analysis further confirmed stable forward flow through the prosthetic valve. Blood entered the computational domain with a relatively uniform velocity profile before accelerating through the three leaflet channels to form a coherent central jet downstream of the valve. The absence of substantial flow separation or large recirculation regions indicates that the proposed valve geometry promotes organized transvalvular flow under the prescribed physiological conditions.

Unlike FSI simulations, which simultaneously solve the coupled interaction between leaflet deformation and blood flow, the present investigation intentionally employed two independent computational analyses. The finite element model evaluated the structural response of the polyurethane leaflets under physiological pressure loading, whereas the CFD model considered only the blood domain flowing through a prescribed rigid, fully open valve geometry. Consequently, the CFD results represent the intrinsic hemodynamic characteristics of the valve geometry rather than the interaction between blood flow and leaflet motion. This independent computational strategy substantially reduces computational cost while providing valuable preliminary insight into both structural response and transvalvular hemodynamics, making it particularly suitable during the early stages of prosthetic valve design before undertaking computationally intensive FSI analyses or experimental validation [15]. Previous studies have shown that fully coupled FSI models provide the most complete representation of leaflet–flow interaction but require substantially greater computational complexity. Luraghi et al. directly compared structural and FSI simulations of an aortic valve prosthesis and showed that the selected modeling approach should depend on the specific outcome being investigated [25,60]. In this context, the present independent FEA and CFD analyses are intended as preliminary design assessments rather than substitutes for a coupled FSI model.

The present investigation should therefore be interpreted as a preliminary computational design assessment rather than validation of a fundamentally new prosthetic valve architecture. The valve geometry was independently reconstructed using dimensions reported in the literature, while maintaining design flexibility for computational evaluation. The independent structural and hemodynamic analyses provide geometry-specific information regarding leaflet deformation, commissural stress localization, transvalvular jet formation, turbulent kinetic energy, and wall shear stress distributions. These findings establish a computational baseline for subsequent geometric optimization, experimental validation, and future fluid–structure interaction studies.

4.1. Limitations

Several limitations should be considered when interpreting the findings of this study. First, the structural and fluid simulations were performed independently rather than using a fully coupled FSI framework. Consequently, the CFD analysis was conducted using a fixed-open valve geometry and does not account for the influence of leaflet deformation on the surrounding blood flow. Second, blood was modeled as an incompressible Newtonian fluid, which is an acceptable approximation for large-vessel aortic flow but does not capture the non-Newtonian behavior [61] that may occur at lower shear rates. Third, the valve geometry represents an idealized prosthetic design rather than a patient-specific anatomy, and only a single valve size was investigated. Finally, the computational predictions have not yet been validated experimentally or through in vitro hydrodynamic testing. Furthermore, the present investigation evaluated only a single polyurethane prosthetic valve geometry and did not include direct comparison with commercially available surgical or transcatheter prosthetic valve designs.

The leaflet material was treated as homogeneous, isotropic, and linear elastic, so viscoelasticity, nonlinear hyperelastic response, anisotropy, damage, and fatigue are not represented [29]. The rigid fixed-open CFD model cannot describe opening and closing dynamics, regurgitation, leaflet flutter, or the coupling between leaflet deformation and flow, and no conclusion on these phenomena or on long-term durability is drawn. Luraghi et al. found that the geometric orifice area of a polymeric valve differed from in vitro measurements by 5% in an FSI model and by 46.5% in a structural finite element model [25], so the fixed-open geometry assumed here may not match the orifice area reached in operation. Plane-averaged upstream and downstream pressures were not extracted, so the reported 38.44 mmHg magnitude-based and 34.34 mmHg axial-component-based Bernoulli estimates are not directly computed transvalvular pressure differences.

Despite these limitations, the independent FEA and CFD analyses provide a preliminary computational framework for evaluating the structural and hemodynamic performance of polymeric prosthetic valves during the early stages of design and optimization.

4.2. Future Work

Future investigations should incorporate geometric optimization of the leaflet design, fully coupled fluid–structure interaction simulations, patient-specific valve geometries, non-Newtonian blood rheology, hyperelastic and viscoelastic leaflet material models calibrated to tensile tests, turbulence-model sensitivity, in vitro pulse-duplicator testing under ISO 5840-2 [59], comparison with commercially available valves, fatigue and durability analyses [62] and experimental validation to further evaluate long-term prosthetic valve performance under physiological and pathological conditions, including systemic hypertension and left ventricular hypertrophy.

5. Conclusions

This study presented an independent computational framework consisting of separate finite element analysis and computational fluid dynamics simulations to evaluate the structural and hemodynamic performance of an independently reconstructed polyurethane prosthetic aortic valve. Although the valve dimensions were derived from published physiological data, the computational framework enabled systematic assessment of geometry-specific mechanical and flow characteristics during the preliminary stages of valve development.

The predicted leaflet response and flow characteristics indicate that the proposed geometry is a candidate for further computational optimization and experimental investigation. The results do not establish structural integrity, durability, or clinical suitability,

which require coupled FSI analysis, fatigue analysis, and in vitro testing. Furthermore, the independent FEA and CFD framework established in this study provides a reproducible computational framework that can support iterative prosthetic valve design optimization, guide experimental prototype development, and facilitate subsequent fluid–structure interaction and in vitro validation studies.

Author Contributions: Conceptualization, T.G.; methodology, C.B.S., S.N. and T.G.; software, C.B.S., S.N. and T.G.; validation, C.B.S., S.N. and T.G.; formal analysis, S.N.; investigation, C.B.S., S.N. and T.G.; resources, T.G.; data curation, C.B.S. and T.G.; writing—original draft, C.B.S. and S.N.; writing—review and editing, S.N. and T.G.; visualization, C.B.S., S.N. and T.G.; supervision, S.N. and T.G.; project administration, T.G.; funding acquisition, T.G. All authors have read and agreed to the published version of the manuscript.

Funding: This research received no external funding.

Institutional Review Board Statement: Not applicable. This study involved computational simulations and did not include human participants or identifiable human data.

Informed Consent Statement: Not applicable. This study did not involve human participants.

Data Availability Statement: The original contributions presented in this study are included in the article. Further inquiries can be directed to the corresponding author.

Conflicts of Interest: The authors declare no conflicts of interest.

References

1. Otto, C.M.; Nishimura, R.A.; Bonow, R.O.; Carabello, B.A.; Erwin, J.P.; Gentile, F.; Jneid, H.; Krieger, E.V.; Mack, M.; McLeod, C.; et al. 2020 ACC/AHA Guideline for the Management of Patients With Valvular Heart Disease: A Report of the American College of Cardiology/American Heart Association Joint Committee on Clinical Practice Guidelines. *Circulation* **2021**, *143*, e35–e71. https://doi.org/10.1161/CIR.0000000000000923.
2. Vahanian, A.; Beyersdorf, F.; Praz, F.; Milojevic, M.; Baldus, S.; Bauersachs, J.; Capodanno, D.; Conradi, L.; De Bonis, M.; De Paulis, R.; et al. 2021 ESC/EACTS Guidelines for the Management of Valvular Heart Disease. *Eur. Heart J.* **2022**, *43*, 561–632. https://doi.org/10.1093/eurheartj/ehab395.
3. Sacks, M.S.; Schoen, F.J.; Mayer, J.E. Bioengineering Challenges for Heart Valve Tissue Engineering. *Annu. Rev. Biomed. Eng.* **2009**, *11*, 289–313. https://doi.org/10.1146/annurev-bioeng-061008-124903.
4. Michelena, H.I.; Corte, A.D.; Prakash, S.K.; Milewicz, D.M.; Evangelista, A.; Enriquez-Sarano, M. Bicuspid Aortic Valve Aortopathy in Adults: Incidence, Etiology, and Clinical Significance. *Int. J. Cardiol.* **2015**, *201*, 400–407.
5. Head, S.J.; Mokhles, M.M.; Osnabrugge, R.L.J.; Pibarot, P.; Mack, M.J.; Takkenberg, J.J.M.; Bogers, A.J.J.C.; Kappetein, A.P. The Impact of Prosthesis–Patient Mismatch on Long-Term Survival after Aortic Valve Replacement: A Systematic Review and Meta-Analysis of 34 Observational Studies Comprising 27 186 Patients with 133 141 Patient-Years. *Eur. Heart J.* **2012**, *33*, 1518–1529. https://doi.org/10.1093/eurheartj/ehs003.
6. Bourguignon, T.; Bouquiaux-Stablo, A.-L.; Candolfi, P.; Mirza, A.; Loardi, C.; May, M.-A.; El-Khoury, R.; Marchand, M.; Aupart, M. Very Long-Term Outcomes of the Carpentier-Edwards Perimount Valve in Aortic Position. *Ann. Thorac. Surg.* **2015**, *99*, 831–837. https://doi.org/10.1016/j.athoracsur.2014.09.030.
7. Singh, S.K.; Kachel, M.; Castillero, E.; Xue, Y.; Kalfa, D.; Ferrari, G.; George, I. Polymeric Prosthetic Heart Valves: A Review of Current Technologies and Future Directions. *Front. Cardiovasc. Med.* **2023**, *10*, 1137827. https://doi.org/10.3389/fcvm.2023.1137827.
8. Wang, Y.; Fu, Y.; Wang, Q.; Kong, D.; Wang, Z.; Liu, J. Recent Advancements in Polymeric Heart Valves: From Basic Research to Clinical Trials. *Mater. Today Bio* **2024**, *28*, 101194. https://doi.org/10.1016/j.mtbio.2024.101194.
9. Melo, S.F.; Nondonfaz, A.; Aqil, A.; Pierrard, A.; Hulin, A.; Delierneux, C.; Ditkowski, B.; Gustin, M.; Legrand, M.; Tullemans, B.M.E.; et al. Design, Manufacturing and Testing of a Green Non-Isocyanate Polyurethane Prosthetic Heart Valve. *Biomater. Sci.* **2024**, *12*, 2149–2164. https://doi.org/10.1039/D3BM01911J.
10. Miri, Z.; Farè, S.; Ma, Q.; Haugen, H.J. Updates on Polyurethane and Its Multifunctional Applications in Biomedical Engineering. *Prog. Biomed. Eng.* **2023**, *5*, 042001. https://doi.org/10.1088/2516-1091/acef84.

11. Bernacca, G.M.; O'Connor, B.; Williams, D.F.; Wheatley, D.J. Hydrodynamic Function of Polyurethane Prosthetic Heart Valves: Influences of Young's Modulus and Leaflet Thickness. *Biomaterials* **2002**, *23*, 45–50. https://doi.org/10.1016/S0142-9612(01)00077-1.
12. Heitkemper, M.; Hatoum, H.; Dasi, L.P. In Vitro Hemodynamic Assessment of a Novel Polymeric Transcatheter Aortic Valve. *J. Mech. Behav. Biomed. Mater.* **2019**, *98*, 163–171. https://doi.org/10.1016/j.jmbbm.2019.06.016.
13. Rotman, O.M.; Kovarovic, B.; Bianchi, M.; Slepian, M.J.; Bluestein, D. In Vitro Durability and Stability Testing of a Novel Polymeric Transcatheter Aortic Valve. *ASAIO J.* **2020**, *66*, 190–198. https://doi.org/10.1097/MAT.0000000000000980.
14. Sun, W.; Martin, C.; Pham, T. Computational Modeling of Cardiac Valve Function and Intervention. *Annu. Rev. Biomed. Eng.* **2014**, *16*, 53–76. https://doi.org/10.1146/annurev-bioeng-071813-104517.
15. Šeman, M.; Stephens, A.F.; Kaye, D.M.; Gregory, S.D.; Stub, D. Computational Modelling of Valvular Heart Disease: Haemodynamic Insights and Clinical Implications. *Front. Bioeng. Biotechnol.* **2024**, *12*, 1462542. https://doi.org/10.3389/fbioe.2024.1462542.
16. Fumagalli, I.; Pagani, S.; Vergara, C.; Dede', L.; Adebo, D.A.; Del Greco, M.; Frontera, A.; Luciani, G.B.; Pontone, G.; Scrofani, R.; et al. The Role of Computational Methods in Cardiovascular Medicine: A Narrative Review. *Transl. Pediatr.* **2024**, *13*, 146–163. https://doi.org/10.21037/tp-23-184.
17. Toma, M.; Singh-Gryzbon, S.; Frankini, E.; Wei, Z.; Yoganathan, A.P. Clinical Impact of Computational Heart Valve Models. *Materials* **2022**, *15*, 3302. https://doi.org/10.3390/ma15093302.
18. Yoganathan, A.P.; He, Z.; Jones, S.C. Fluid Mechanics of Heart Valves. *Annu. Rev. Biomed. Eng.* **2004**, *6*, 331–362.
19. Dasi, L.P.; Simon, H.A.; Sucosky, P.; Yoganathan, A.P. FLUID MECHANICS OF ARTIFICIAL HEART VALVES. *Clin. Exp. Pharmacol. Physiol.* **2009**, *36*, 225–237. https://doi.org/10.1111/j.1440-1681.2008.05099.x.
20. Sotiropoulos, F.; Le, T.B.; Gilmanov, A. Fluid Mechanics of Heart Valves and Their Replacements. *Annu. Rev. Fluid Mech.* **2016**, *48*, 259–283. https://doi.org/10.1146/annurev-fluid-122414-034314.
21. Fan, Q.; Qi, D.; Ren, L.; Xiao, Q.; Zhou, X. Mechanical Characterization and Materials Modeling Frameworks for Prosthetic Heart Valves: Investigations and Future Directions in Computational Biomechanics. *Comput. Methods Biomech. Biomed. Engin.* **2025**, 1–53. https://doi.org/10.1080/10255842.2025.2595136.
22. Votta, E.; Le, T.B.; Stevanella, M.; Fusini, L.; Caiani, E.G.; Redaelli, A.; Sotiropoulos, F. Toward Patient-Specific Simulations of Cardiac Valves: State-of-the-Art and Future Directions. *J. Biomech.* **2013**, *46*, 217–228. https://doi.org/10.1016/j.jbiomech.2012.10.026.
23. Marom, G.; Haj-Ali, R.; Raanani, E.; Schäfers, H.-J.; Rosenfeld, M. A Fluid–Structure Interaction Model of the Aortic Valve with Coaptation and Compliant Aortic Root. *Med. Biol. Eng. Comput.* **2012**, *50*, 173–182. https://doi.org/10.1007/s11517-011-0849-5.
24. Hsu, M.-C.; Kamensky, D.; Bazilevs, Y.; Sacks, M.S.; Hughes, T.J.R. Fluid–Structure Interaction Analysis of Bioprosthetic Heart Valves: Significance of Arterial Wall Deformation. *Comput. Mech.* **2014**, *54*, 1055–1071. https://doi.org/10.1007/s00466-014-1059-4.
25. Luraghi, G.; Wu, W.; De Gaetano, F.; Rodriguez Matas, J.F.; Moggridge, G.D.; Serrani, M.; Stasiak, J.; Costantino, M.L.; Migliavacca, F. Evaluation of an Aortic Valve Prosthesis: Fluid-Structure Interaction or Structural Simulation? *J. Biomech.* **2017**, *58*, 45–51. https://doi.org/10.1016/j.jbiomech.2017.04.004.
26. Bavo, A.M.; Rocatello, G.; Iannaccone, F.; Degroote, J.; Vierendeels, J.; Segers, P. Fluid-Structure Interaction Simulation of Prosthetic Aortic Valves: Comparison between Immersed Boundary and Arbitrary Lagrangian-Eulerian Techniques for the Mesh Representation. *PLoS ONE* **2016**, *11*, e0154517. https://doi.org/10.1371/journal.pone.0154517.
27. Reul, H.; Vahlbruch, A.; Giersiepen, M.; Schmitz-Rode, T.; Hirtz, V.; Effert, S. The Geometry of the Aortic Root in Health, at Valve Disease and after Valve Replacement. *J. Biomech.* **1990**, *23*, 181–191. https://doi.org/10.1016/0021-9290(90)90351-3.
28. Labrosse, M.R.; Beller, C.J.; Robicsek, F.; Thubrikar, M.J. Geometric Modeling of Functional Trileaflet Aortic Valves: Development and Clinical Applications. *J. Biomech.* **2006**, *39*, 2665–2672. https://doi.org/10.1016/j.jbiomech.2005.08.012.
29. Kanyanta, V.; Ivankovic, A. Mechanical Characterisation of Polyurethane Elastomer for Biomedical Applications. *J. Mech. Behav. Biomed. Mater.* **2010**, *3*, 51–62. https://doi.org/10.1016/j.jmbbm.2009.03.005.
30. Li, K.; Sun, W. Simulated Transcatheter Aortic Valve Deformation: A Parametric Study on the Impact of Leaflet Geometry on Valve Peak Stress. *Int. J. Numer. Methods Biomed. Eng.* **2017**, *33*, e02814. https://doi.org/10.1002/cnm.2814.
31. Makhijani, V.B.; Yang, H.Q.; Dionne, P.J.; Thubrikar, M.J. Three-Dimensional Coupled Fluid-Structure Simulation of Pericardial Bioprosthetic Aortic Valve Function. *ASAIO J.* **1997**, *43*, M387–M392.

32. Kamensky, D.; Hsu, M.-C.; Schillinger, D.; Evans, J.A.; Aggarwal, A.; Bazilevs, Y.; Sacks, M.S.; Hughes, T.J.R. An Immersogeometric Variational Framework for Fluid–Structure Interaction: Application to Bioprosthetic Heart Valves. *Comput. Methods Appl. Mech. Eng.* **2015**, *284*, 1005–1053. https://doi.org/10.1016/j.cma.2014.10.040.
33. Becsek, B.; Pietrasanta, L.; Obrist, D. Turbulent Systolic Flow Downstream of a Bioprosthetic Aortic Valve: Velocity Spectra, Wall Shear Stresses, and Turbulent Dissipation Rates. *Front. Physiol.* **2020**, *11*, 577188. https://doi.org/10.3389/fphys.2020.577188.
34. Bennati, L.; Crispino, A.; Vergara, C. Computational Modeling of Cardiac Hemodynamics Including Chordae Tendineae, Papillaries, and Valves Dynamics. *Comput. Biol. Med.* **2025**, *186*, 109658. https://doi.org/10.1016/j.compbiomed.2025.109658.
35. Brambila-Solórzano, A.; Méndez-Lavielle, F.; Naude, J.L.; Martínez-Sánchez, G.J.; García-Rebolledo, A.; Hernández, B.; Escobar-del Pozo, C. Influence of Blood Rheology and Turbulence Models in the Numerical Simulation of Aneurysms. *Bioengineering* **2023**, *10*, 1170. https://doi.org/10.3390/bioengineering10101170.
36. Canbolat, G.; Etli, M.; Karahan, O.; Koru, M.; Korkmaz, E. Investigation of vascular flow in a thoracic aorta in terms of flow models and blood rheology via computational fluid dynamics (CFD). *J. Mech. Med. Biol.* **2024**, *24*, 4. https://doi.org/10.1142/S021951942350094X.
37. Madhavan, S.; Kemmerling, E.M.C. The Effect of Inlet and Outlet Boundary Conditions in Image-Based CFD Modeling of Aortic Flow. *Biomed. Eng. Online* **2018**, *17*, 66. https://doi.org/10.1186/s12938-018-0497-1.
38. Vennin, S.; Mayer, A.; Li, Y.; Fok, H.; Clapp, B.; Alastruey, J.; Chowienczyk, P. Noninvasive Calculation of the Aortic Blood Pressure Waveform from the Flow Velocity Waveform: A Proof of Concept. *Am. J. Physiol.-Heart Circ. Physiol.* **2015**, *309*, H969–H976. https://doi.org/10.1152/ajpheart.00152.2015.
39. Black, S.M.; Maclean, C.; Hall Barrientos, P.; Ritos, K.; McQueen, A.; Kazakidi, A. Calibration of Patient-Specific Boundary Conditions for Coupled CFD Models of the Aorta Derived from 4D Flow-MRI. *Front. Bioeng. Biotechnol.* **2023**, *11*, 1178483. https://doi.org/10.3389/fbioe.2023.1178483.
40. Su, B.; Craven, B.A.; Kubicki, C.J.; Khalil, D.; Simon, S.D.; Manning, K.B. Computational Modeling of Flow in an in Vitro Cerebrovascular Model Under Pulsatile Conditions with Experimental Validation. *Cardiovasc. Eng. Technol.* **2026**, *17*, 76–84. https://doi.org/10.1007/s13239-025-00813-x.
41. Arminio, M.; Carbonaro, D.; Morbiducci, U.; Gallo, D.; Chiastra, C. Fluid-Structure Interaction Simulation of Mechanical Aortic Valves: A Narrative Review Exploring Its Role in Total Product Life Cycle. *Front. Med. Technol.* **2024**, *6*, 1399729. https://doi.org/10.3389/fmedt.2024.1399729.
42. Celik, I.; Ghia, U.; Roache, P.J.; Freitas, C.; Coloman, H.; Raad, P.E. Procedure for Estimation and Reporting of Uncertainty Due to Discretization in CFD Applications. *J. Fluids Eng.* **2008**, *130*, 078001. https://doi.org/10.1115/1.2960953.
43. Zhou, J.; Li, Y.; Li, T.; Tian, X.; Xiong, Y.; Chen, Y. Analysis of the Effect of Thickness on the Performance of Polymeric Heart Valves. *J. Funct. Biomater.* **2023**, *14*, 309. https://doi.org/10.3390/jfb14060309.
44. Masheane, L.R.; du Preez, W.; Combrinck, J. Evaluation of the Impact of Stress Distribution on Polyurethane Trileaflet Heart Valve Leaflets in the Open Configuration by Employing Numerical Simulation. *Math. Comput. Appl.* **2024**, *29*, 64. https://doi.org/10.3390/mca29040064.
45. Hatoum, H.; Yousefi, A.; Lilly, S.; Maureira, P.; Crestanello, J.; Dasi, L.P. An in Vitro Evaluation of Turbulence after Transcatheter Aortic Valve Implantation. *J. Thorac. Cardiovasc. Surg.* **2018**, *156*, 1837–1848. https://doi.org/10.1016/j.jtcvs.2018.05.042.
46. Klyshnikov, K.Y.; Onischenko, P.S.; Ovcharenko, E.A. Study of Biomechanics of the Heart Valve Leaflet Apparatus Using Numerical Simulation Method. *Sovrem. Tehnol. Med.* **2022**, *14*, 6. https://doi.org/10.17691/stm2022.14.2.01.
47. Stanová, V.; Rieu, R.; Thollon, L.; Salaun, E.; Rodés-Cabau, J.; Côté, N.; Mantovani, D.; Pibarot, P. Leaflet Mechanical Stress in Different Designs and Generations of Transcatheter Aortic Valves: An in Vitro Study. *Struct. Heart* **2024**, *8*, 100262. https://doi.org/10.1016/j.shj.2023.100262.
48. Meng, Z.; Zhang, H.; Cai, Y.; Gao, Y.; Liang, C.; Wang, J.; Chen, X.; Guo, L.; Wang, S. Computational Study of Transcatheter Aortic Valve Replacement Based on Patient-Specific Models—Rapid Surgical Planning for Self-Expanding Valves. *Front. Physiol.* **2024**, *15*, 1407215. https://doi.org/10.3389/fphys.2024.1407215.
49. Wu, W.; Pott, D.; Mazza, B.; Sironi, T.; Dordoni, E.; Chiastra, C.; Petrini, L.; Pennati, G.; Dubini, G.; Steinseifer, U.; et al. Fluid–Structure Interaction Model of a Percutaneous Aortic Valve: Comparison with an In Vitro Test and Feasibility Study in a Patient-Specific Case. *Ann. Biomed. Eng.* **2016**, *44*, 590–603. https://doi.org/10.1007/s10439-015-1429-x.
50. Claiborne, T.E.; Sheriff, J.; Kuetting, M.; Steinseifer, U.; Slepian, M.J.; Bluestein, D. In Vitro Evaluation of a Novel Hemodynamically Optimized Trileaflet Polymeric Prosthetic Heart Valve. *J. Biomech. Eng.* **2013**, *135*, 021021. https://doi.org/10.1115/1.4023235.

51. De Gaetano, F.; Bagnoli, P.; Zaffora, A.; Pandolfi, A.; Serrani, M.; Brubert, J.; Stasiak, J.; Moggridge, G.D.; Costantino, M.L. A newly developed tri-leaflet polymeric heart valve prosthesis. *J. Mech. Med. Biol.* **2015**, *15*, 1540009. https://doi.org/10.1142/S0219519415400096.
52. Stanfield, J.R.; Johnson, G.; Belais, N.; George, I.; Yakubov, S. Development and Preclinical Results of a Transcatheter Aortic Valve Implant with Novel Polymeric Leaflets. *npj Cardiovasc. Health* **2026**, *3*, 14. https://doi.org/10.1038/s44325-026-00112-x.
53. Rezvova, M.A.; Klyshnikov, K.Y.; Gritskevich, A.A.; Ovcharenko, E.A. Polymeric Heart Valves Will Displace Mechanical and Tissue Heart Valves: A New Era for the Medical Devices. *Int. J. Mol. Sci.* **2023**, *24*, 3963.
54. Rotman, O.M.; Kovarovic, B.; Chiu, W.-C.; Bianchi, M.; Marom, G.; Slepian, M.J.; Bluestein, D. Novel Polymeric Valve for Transcatheter Aortic Valve Replacement Applications: In Vitro Hemodynamic Study. *Ann. Biomed. Eng.* **2019**, *47*, 113–125. https://doi.org/10.1007/s10439-018-02119-7.
55. Lee, A.; Liu, X.; Giaretta, J.E.; Hoang, T.P.; Crago, M.; Farajikhah, S.; Mosse, L.; Fletcher, D.F.; Dehghani, F.; Winlaw, D.S.; et al. Bioinspired Polymeric Heart Valves: A Combined in Vitro and in Silico Approach. *JTCVS Open* **2023**, *15*, 113–124. https://doi.org/10.1016/j.xjon.2023.06.020.
56. Dumont, K.; Stijnen, J.M.A.; Vierendeels, J.; van de Vosse, F.N.; Verdonck, P.R. Validation of a Fluid–Structure Interaction Model of a Heart Valve Using the Dynamic Mesh Method in Fluent. *Comput. Methods Biomech. Biomed. Engin.* **2004**, *7*, 139–146. https://doi.org/10.1080/10255840410001715222.
57. Soni, P.; Kumar, S.; Kumar, B.V.R.; Rai, S.K.; Verma, A.; Shankar, O. A Comprehensive Review on CFD Simulations of Left Ventricle Hemodynamics: Numerical Methods, Experimental Validation Techniques, and Emerging Trends. *J. Braz. Soc. Mech. Sci. Eng.* **2024**, *46*, 301. https://doi.org/10.1007/s40430-024-04875-1.
58. Canbolat, G.; Daricik, F.; Koru, M.; Karahan, O. Experimental and Numerical Investigation of Patient-Specific Hemodynamics in the Thoracic Aorta Using the CFD Method with Newtonian Blood Flow Assumption. *Sādhanā* **2026**, *51*, 298. https://doi.org/10.1007/s12046-026-03284-5.
59. *ISO 5840-2:2021*; Cardiovascular Implants—Cardiac Valve Prostheses—Part 2: Surgically Implanted Heart Valve Sub-Stitutes. International Organization for Standardization: Geneva, Switzerland, 2021.
60. Xu, F.; Morganti, S.; Zakerzadeh, R.; Kamensky, D.; Auricchio, F.; Reali, A.; Hughes, T.J.R.; Sacks, M.S.; Hsu, M. A Framework for Designing Patient-specific Bioprosthetic Heart Valves Using Immersogeometric Fluid–Structure Interaction Analysis. *Int. J. Numer. Methods Biomed. Eng.* **2018**, *34*, e2938. https://doi.org/10.1002/cnm.2938.
61. De Vita, F.; de Tullio, M.D.; Verzicco, R. Numerical Simulation of the Non-Newtonian Blood Flow through a Mechanical Aortic Valve. *Theor. Comput. Fluid Dyn.* **2016**, *30*, 129–138. https://doi.org/10.1007/s00162-015-0369-2.
62. Martin, C.; Sun, W. Simulation of Long-Term Fatigue Damage in Bioprosthetic Heart Valves: Effects of Leaflet and Stent Elastic Properties. *Biomech. Model. Mechanobiol.* **2014**, *13*, 759–770. https://doi.org/10.1007/s10237-013-0532-x.

Disclaimer/Publisher's Note: The statements, opinions and data contained in all publications are solely those of the individual author(s) and contributor(s) and not of MDPI and/or the editor(s). MDPI and/or the editor(s) disclaim responsibility for any injury to people or property resulting from any ideas, methods, instructions or products referred to in the content.